Journal of Applied Physics

# Analytical model of low and high ablation regimes in carbon arcs

Cite as: J. Appl. Phys. **128**, 123303 (2020); https://doi.org/10.1063/5.0016110
Submitted: 01 June 2020 . Accepted: 08 September 2020 . Published Online: 29 September 2020

A. Khrabry, I. D. Kaganovich, A. Khodak, V. Vekselman, and T. Huang



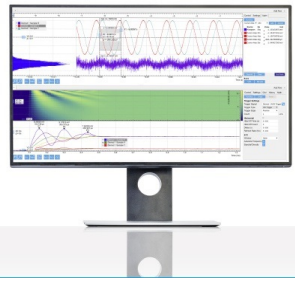







AIP Publishing

Journal of Applied Physics ARTICLE scitation.org/journal/jap

# Analytical model of low and high ablation regimes in carbon arcs

Cite as: J. Appl. Phys. **128**, 123303 (2020); doi: 10.1063/5.0016110
Submitted: 1 June 2020 · Accepted: 8 September 2020 ·
Published Online: 29 September 2020



A. Khrabry,[a),b)] I. D. Kaganovich, A. Khodak, V. Vekselman,[c)] and T. Huang[d)]

## AFFILIATIONS

Princeton Plasma Physics Laboratory, 100 Stellarator Road, Princeton, New Jersey 08542, USA

**Note:** This paper is part of the Special Topic on Fundamentals and Applications of Atmospheric Pressure Plasmas

[a)]**Author to whom correspondence should be addressed:** akhrabry@pppl.gov

[b)]**Present address:** Lawrence Livermore National Laboratory (LLNL), 7000 East Ave, Livermore, CA 94550, USA. LLNL is operated by Lawrence Livermore National Security, LLC, for the U.S. Department of Energy, National Nuclear Security Administration under Contract DE-AC52-07NA27344.

[c)]**Present address:** University of California Irvine (UCI), Irvine, CA 92697, USA.

[d)]**Present address:** College of Physics and Optoelectronic Engineering, Shenzhen University, 3688 Nanhai Boulevard, Nanshan, Shenzhen 518060, China.

## ABSTRACT

Graphite ablation by an electric arc or a laser/solar flux is widely used for the synthesis of carbon nanomaterials. Previously, it was observed in multiple arc experiments that the ablation rate is a strong nonlinear function of the arc current and it drastically increases at some threshold current. We developed an analytical model explaining this transition in the rate of ablation by an electric arc or a laser/solar flux. The model not only explains the observations but can also accurately predict the experimentally observed ablation rates. The model takes into account redeposition of carbon back to the ablated surface, which is the key process responsible for the observed effects.



## I. INTRODUCTION

Gas-phase production of carbon nanoparticles is often based on evaporation of bulk solid graphite into an atmosphere of an inert background gas, where evaporated carbon condenses and serves as a feedstock for the nanoparticle growth.[1–11] An electric arc[1–4] or a laser/focused solar light beam[6–8,12] is utilized as a heat source for the ablation. In particular, the electric arc with graphite electrodes (i.e., carbon arc) is known as an inexpensive and scalable method to produce high-quality carbon nanotubes.[13–15] The ablation rate of a graphite anode is an important characteristic of the synthesis process that determines the synthesis yield and affects the gas phase conditions for the growth of the nanoparticles such as gas composition, temperature, and residence time.

Multiple experiments have been conducted with carbon arcs for nano-synthesis.[4,16–18] In these experiments, arcs were run between two coaxial cylindrical electrodes in an atmosphere of helium at 67 kPa (500 Torr). Radii of electrodes and their separation were varied as well as the arc current. Experiments showed that the ablation rate of the graphite anode is a complex function of the arc parameters; two distinguishable regimes were observed: high and low ablation regimes. As an example, experimental data[18] on the ablation rate as a function of arc current at a fixed anode size and electrode separation are plotted in Fig. 1. At a low current, the ablation rate is low and weakly depends on the arc parameters (this is a low ablation regime). However, when the arc current exceeds a certain value, the ablation rate increases rapidly with the arc current (this is a high ablation regime). Similar behavior of the ablation rate, with low ablation and high ablation regimes, was also observed for the variation of the anode radius and the inter-electrode gap. A model capable of explaining both ablation regimes and predicting the ablation rate as a function of experimental parameters for an electric arc (or a laser or UV light beam) is needed for planning the experiments and to better control the synthesis process.

Multiple computational and theoretical models have been developed for carbon arcs.[2,17,19–21] However, these models had a focus on the arc plasma rather than on the ablation rate: ablation

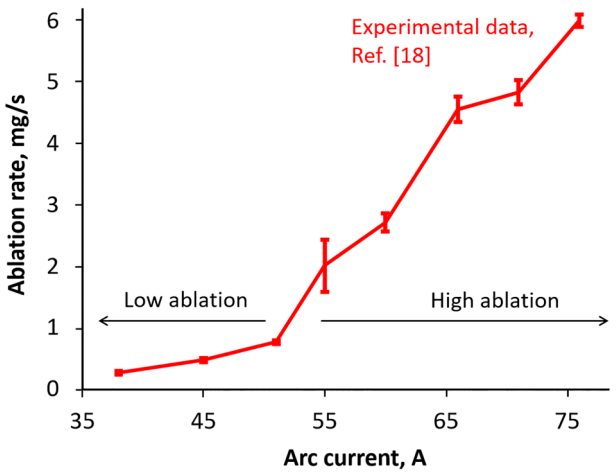


**FIG. 1.** Anode ablation rate as a function of arc current. Experimental data from Ref. [18]. Electrode separation d and radii $r_a$, $r_c$ were kept constant (d = 1.5 mm, $r_a$ = 3 mm, $r_c$ = 4.5 mm).

rate was either pre-defined or was estimated using Langmuir's law[22] for evaporation in vacuum. As a result, these models cannot describe and predict both high and low ablation regimes with a rapid transition between them. It is known that the presence of background gas can substantially limit the outflow of the evaporated material from the evaporation surface,[9,23] thereby reducing the ablation rate. Our latest model[24] has a more accurate expression for the ablation rate that accounts for the presence of the background gas; however, the results were obtained for the low ablation regime only. In a recent paper,[25] the background pressure is taken into account in the modeling of copper anode evaporation.

In this paper, we theoretically explain that the presence of a background gas plays a crucial role in the formation of two ablation regimes observed in the experiments. We derive an ablation model based on the heat balance in between a plasma and an electrode (or a target for the light beam) and provide analytical expressions for the ablation rate of a thin cylindrical electrode.

The paper is organized as follows. In Sec. II, the ablation model accounting for the presence of a background gas is described; an explanation for the low and high ablation regimes is given; analytical expressions for the ablation flux and the surface temperature corresponding to the transition between two ablation regimes are derived. Section III provides the validation of the ablation model by comparison to the available experimental data on the ablation rate as a function of the surface temperature. In Sec. IV, a model to determine the anode ablation rate from the energy balance in a carbon arc is described. Section V presents analytical expressions for the ablation rate in high and low ablation regimes which are derived as functions of the arc parameters. In Sec. VI, numerical and analytical solutions are validated via comparison to vast experimental data on the anode ablation rate in carbon arcs with various arc currents, electrode separation distances, and anode radii. Section VII contains a summary of the work.

## II. THE ABLATION MODEL

### A. Ablation in the presence of a background gas

In the case of ablation in a vacuum, a flux of ablated material from a surface is given by Langmuir's formula,[22]

$$g_{abl}(T_a) = p_{sat,C}(T_a)/v_{th}, \quad v_{th} = \sqrt{2\pi k T_a/m_C}. \tag{1}$$

Here, $m_C$ is the mass of ablated particles (carbon atoms or molecules), $k$ is the Boltzmann constant, $T_a$ is the surface temperature, and $p_{sat,C}(T_a)$ is the saturation pressure of carbon given by the Clausius–Clapeyron relation,

$$p_{sat,C}(T_a) = p_0 \exp\left(-\frac{Lm_C}{kT_a}\right), \tag{2}$$

where $L$ is the latent heat of graphite ablation and $p_0$ is a material-dependent constant. Values of the ablation flux parameters $L$, $m_C$, and $p_0$ are discussed in Appendix A and are also summarized in Appendix C.

If there is a background gas, it will impede the flow of the ablated material away from the ablating surface,[9,23] leading to its accumulation near the surface. This will create a returning flux of the ablated material back to the evaporation surface reducing the net ablation flux,[24,26]

$$g_{abl} = (p_{sat,C}(T_a) - p_{C,a})/v_{th}. \tag{3}$$

Here, $p_{C,a}$ is the partial pressure of carbon vapor at the ablating surface which is determined by the diffusion of the ablated material through the background gas and the ablation flux, $g_{abl}$. As evident from Eq. (3), the background gas can notably affect the net ablation flux via a buildup of the near-surface carbon pressure $p_{C,a}$.

Typically, in nano-synthesis arcs or light-beam (laser) ablation systems, condensation of the ablated carbon takes place rather close to the ablating surface [see Fig. 2(b)]. In electric arcs, most of the ablated material deposits at a closely located cathode.[18,24] In laser-ablation systems, the temperature rapidly decays (on a scale of about 1 mm[8]) below the saturation point

$$T_{sat} = -Lm_C/[k\ln(p/p_0)]. \tag{4}$$

The rapid temperature decay leads to a fast carbon vapor condensation. In other words, the diffusion length is smaller than the ablation surface width. This allows employing a one-dimensional (1D) formulation for the diffusion of carbon. A constant carbon flux, $g_{abl}$, is driven through stationary helium by a gradient of the carbon pressure, as described by the Stefan–Maxwell equation[27–30] (see Appendix B for details),

$$\frac{dp_C}{dx} = -\frac{p_{He}}{nD_{C-He}}\frac{g_{abl}}{m_{C,a}}. \tag{5}$$

Here, $p_C$ and $p_{He}$ are the carbon and helium partial pressures, respectively, $n = p/kT$ is the gas mixture density, and $D_{C-He}$ is the binary diffusion coefficient which can be obtained using the

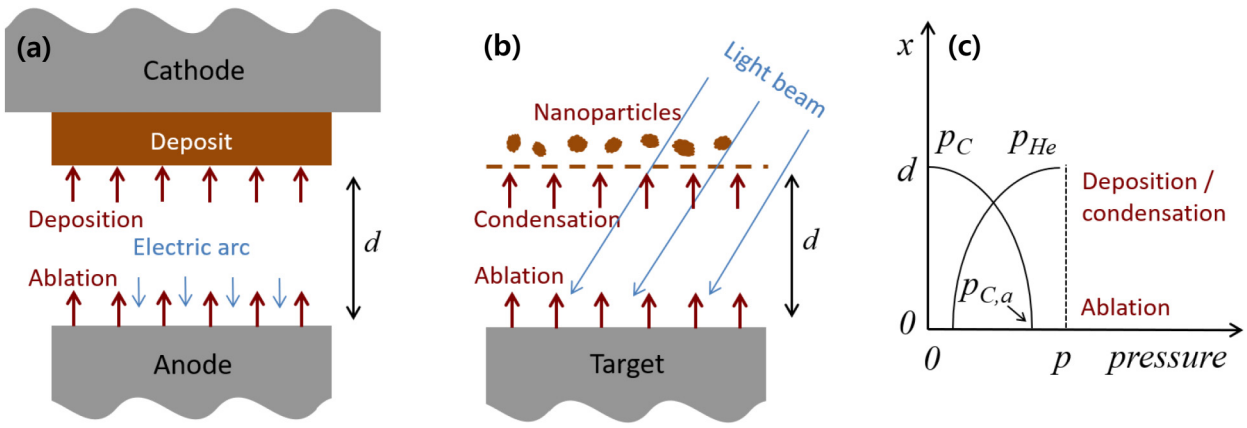


**FIG. 2.** Schematic of carbon transport in an electric arc (a) and a light ablation system (b); schematic profiles of carbon and helium partial pressures (c). Near the ablation surface (x = 0), carbon pressure is at its maximum: $p_C = p_{C,a}$. In the condensation/deposition region, carbon pressure is close to zero. The total pressure in the system is equal to a sum of carbon and helium partial pressures and is constant: $p_C + p_{He} = p = \text{const}$.

kinetic theory of gases,[27–30] and $m_{C,a}$ is the mass of carbon atoms. Carbon molecules are only present in very thin regions near the arc electrodes[43] and, therefore, do not play an important role in the carbon transport in the arc volume. Thereby, only carbon atoms are considered in the carbon transport described by Eq. (5). Note that the denominator $nD_{C-He}$ in the right-hand side of Eq. (5) is a weak function of temperature, as defined by (B2). For typical temperature in an electric arc, $nD_{C-He} = 5 \times 10^{21}\ \text{m}^{-1}\,\text{s}^{-1}$.

As discussed in Appendix B, at conditions typical for the arc and light-beam ablation experiments, the variation of the total pressure $p$ is small, and the fraction of electrons and ions in the gas mixture (the ionization degree) is low. Thereby, the sum of carbon and helium partial pressures $p_C + p_{He} \approx p$ can be taken to be constant, and Eq. (5) can be solved for $p_C$. Zero carbon density can be specified as a boundary condition at the surface opposite to the ablating wall (either a cathode surface in an electric arc or a condensation layer in the laser/solar ablation case, see Fig. 2). A solution of Eq. (5) yields the following carbon gas pressure at the ablating surface:

$$p_{C,a} = p\left[1 - \exp\left(-\frac{g_{abl}}{g_0}\right)\right]. \tag{6}$$

Here, $g_0$ is a characteristic carbon flux determined by the diffusion,

$$g_0 = \frac{m_{C,a} n D_{C-He}}{d}. \tag{7}$$

Here, $d$ is the condensation distance which is either the inter-electrode gap width or a distance to the condensation region in the case of light beam ablation (see Fig. 2). Substitution of (6) into (3) yields the following expression with only one unknown, the ablation flux $g_{abl}$:

$$g_{abl} = \frac{p_{sat,C}(T_a)}{\nu_{th}(T_a)} - \frac{p}{\nu_{th}(T_a)}\left[1 - \exp\left(-\frac{g_{abl}}{g_0}\right)\right]. \tag{8}$$

As predicted by Eq. (8), $g_{abl}$ depends on the surface temperature $T_a$, background pressure $p$, condensation distance $d$, and material properties. Equation (8) can be solved for $g_{abl}$ numerically. The solution of Eq. (8) and the corresponding carbon pressure $p_{C,a}$ are plotted in Fig. 3 with green lines as functions of surface temperature $T_a$ for the background pressure $p = 67$ kPa and two condensation distances $d = 1$ mm and $d = 5$ mm (which cover the range in which the gap was varied in most experiments) corresponding to $g_0 = 0.1\ \text{kg/m}^2\text{/s}$ and $0.02\ \text{kg/m}^2\text{/s}$, respectively.

As evident from the figure, two regimes corresponding to high and low ablation rates can be distinguished with a rapid transition between them. The underlying physics of these regimes is discussed below, and analytical expressions for the surface temperature, ablation flux, and the transition temperature are derived.

Using the fact that $p_{sat,C}$ and $\nu_{th}$ are, respectively, a strong and a weak function of $T_a$, $T_a$ can be explicitly expressed from Eq. (8) as a function of the ablation flux $g_{abl}$ and the background pressure $p$ by substituting a reference value for $T_a = T_{sat}$ in $\nu_{th}$,

$$\frac{1}{T_a} = \frac{1}{T_{sat}} - \frac{k}{L m_C}\ln\left(\frac{g_{abl}}{p}\sqrt{\frac{2\pi k T_{sat}}{m_C}} + \left[1 - \exp\left(-\frac{g_{abl}}{g_0}\right)\right]\right). \tag{9}$$

Here, $T_{sat}$ is the saturation temperature (4). For the temperature range plotted in Fig. 3(a), an error of $T_a$ given by relation (9) is very small, below 4 K.

### B. Low ablation regime

At surface temperatures lower than the saturation temperature of carbon vapor, $T_a < T_{sat}$, and, correspondingly, the carbon vapor

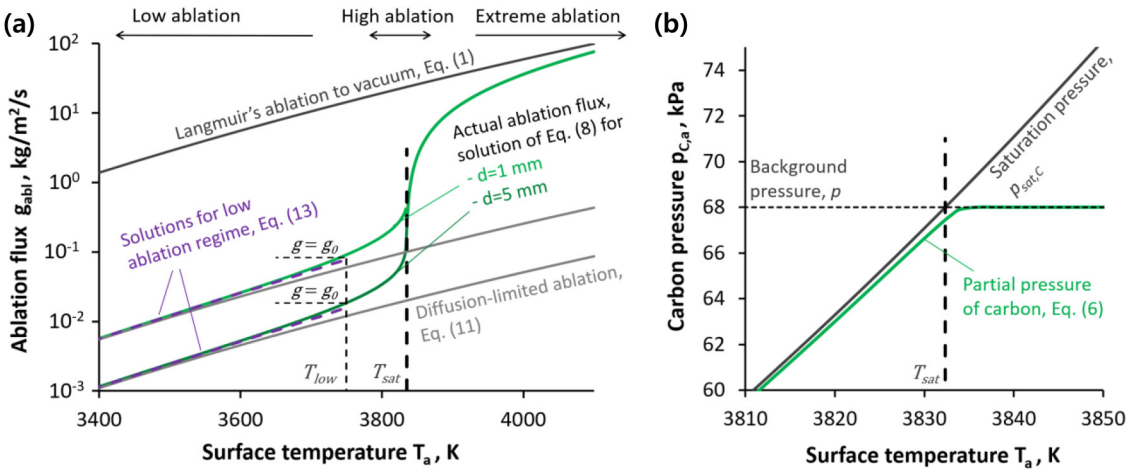


**FIG. 3.** Ablation flux $g_{abl}$ (a) and partial carbon pressure at the surface $p_{C,a}$ (b) as functions of the surface temperature $T_a$ for background pressure p = 67 kPa and condensation distances (inter-electrode gap widths) d = 1 mm and d = 5 mm. Exact numerical solution of Eqs. (6) and (8) are shown by green lines; asymptotic behavior is shown by grey lines. At low temperatures, below the temperature $T_{low}$ given by Eq. (12), the ablation rate is substantially reduced by the presence of background gas, Eq. (11). At high temperatures, above $T_{sat}$ given by Eq. (4), the ablation flux approaches Langmuir's prediction for evaporation to vacuum, Eq. (1).

saturation pressure lower than the system pressure, $p_{sat,C}(T_a) \ll p$, ablation flux is lower than the characteristic diffusive flux, $g_{abl} \ll g_0$. With this, the left-hand side of Eq. (7) can be neglected and the exponent in the right-hand side (RHS) can be linearized yielding

$$g_{abl} \approx g_0 \frac{p_{sat,C}(T_a)}{p}, \tag{10}$$

or, using definition of $g_0$ given by Eq. (6),

$$g_{abl}(T_a) \approx \alpha_{diff} \frac{p_{sat,C}(T_a)}{\nu_{th}}. \tag{11}$$

Here,

$$\alpha_{diff} = \frac{3\pi}{8}\sqrt{\frac{m_{c,a}+m_{He}}{2m_{He}}}\frac{kT}{p\sigma_{c-He}d} = 1.7\frac{kT}{p\sigma_{c-He}d}$$

is the coefficient of ablation flux reduction due to the diffusion of ablated products through the background gas, i.e., helium. Another alternative formulation of Eq. (10) is where $n_0 = \frac{3}{16}\sqrt{2\frac{m_{C,a}+m_{He}}{m_{He}}}\frac{1}{\sigma_{C-j}\,d} = \frac{0.53}{\sigma_{C-j}\,d}$.

As evident from Eq. (10) and Fig. 3(a), the ablation flux is drastically reduced by the background gas at low temperatures. The ablation flux is proportional to the one that would be in the case of ablation in vacuum [Eq. (1)] with a very small factor $\alpha_{diff}$. For typical arc parameters, $d = 2$ mm and $p = 67$ kPa, $\alpha_{diff}$ is about 0.003. The larger is the electrode separation $d$ and the pressure p, the smaller are $\alpha_{diff}$ and the ablation flux.

Figure 3(b) shows the carbon pressure at the surface, $p_{C,a}$ as a function of the surface temperature. As evident from the figure, at $T_a \approx T_{sat}$, the carbon pressure at the surface, $p_{C,a}$ is close to the saturation pressure $p_{sat,C}(T_a)$ for $T_a \le T_{sat}$. This result can be formally obtained by substituting (10) into (6) with a linearized RHS. In this regime, carbon evaporation is almost completely balanced by the redeposition of the ablated material. As a result, the net ablation flux is very low as predicted by Eq. (11).

These conditions correspond to the low ablation regime observed in the arc experiments. As evident from Fig. 3(a), approximations (10) and (11) work reasonably well when the ablation flux is lower than $g_0$. According to Eq. (8) with the LHS neglected, the ablation flux $g_{abl} = g_0$ corresponds to the surface temperature $T_a = T_{low}$ equal to

$$T_{low} = \frac{T_{sat}}{1 + \ln[1 - \exp(-1)] \,/\, \ln(p/p_0)}, \tag{12}$$

where $T_{sat}$ is the saturation temperature (4). Values of $T_{sat}$ and $T_{low}$ for the background pressure used in the arc experiments are given in Appendix C.

The lower is the surface temperature $T_a$ the more accurate is the approximation (10) which was derived from Eq. (8) by linearization of its RHS. For $T_a = T_{low}$ corresponding to $g_{abl} = g_0$, from Eq. (8) it follows that $p_{sat,C}/p = 1 - 1/e$, and an error of Eqs. (10) and (11) is about 40%.

A more accurate expression for the ablation rate can be derived using the second-order Taylor expansion of the exponent in the RHS of Eq. (8),

$$g_{abl} = g_0\left(\frac{p_{sat,C}(T_a)}{p} + \frac{1}{2}\left(\frac{p_{sat,C}(T_a)}{p}\right)^2\right). \tag{13}$$

The results of Eq. (12) are shown in Fig. 3(a) with dashed lines. This approximation works well for surface temperatures up to $T_{low}$.

### C. High ablation regime

The partial pressure of carbon at the surface $p_{C,a}$, apparently, cannot be higher than the background pressure $p$ in the system. When the surface temperature becomes higher than one of carbon saturation, $T_{sat}$, the partial pressure of carbon $p_{C,a}$ reaches its limit $p$ and the deposition flux from the gas can no longer compensate for the ablation flux from the surface. At this point, the net ablation flux grows drastically with the surface temperature, by more than an order of magnitude with the temperature increase of only 10 K, as denoted with a vertical dashed line in Fig. 3(a). This behavior explains the rapid growth of the oblation rate in the high ablation regime, as observed in the experiments.

### D. Extreme ablation regime

At even higher temperatures, $T_a > T_{sat}$, corresponding to $p_{sat,C}(T_a) \gg p$, the carbon pressure at the surface $p_{C,a}$ becomes negligible as compared to $p_{sat,C}$. The ablation flux approaches one given by Langmuir's formula (1) for evaporation in vacuum. For the background pressure of 67 kPa, this regime corresponds to the ablation flux above 10 kg/(m$^2$ s) [see Fig. 3(a)] and flow velocity $v = g_{abl}kT/p_C m_C$ above 400 m/s. At such velocities, the total pressure $p$ must be adjusted to account for fast gas flow with high Mach numbers;, i.e., the constant pressure approximation, $p = const$, cannot be used. However, the carbon pressure will still be negligible as compared to $p_{sat,C}$ in this case. Such an ablation flux corresponds to the ablation rate of 300 mg/s from a 3 mm radius surface (typical radius of an electrode in arc experiments). This regime was not reached in any known arc or laser/solar ablation experiment. For comparison, in experiments from Refs. 4, 8, 17, 18, and 31, maximum ablation rates were below 50 mg/s. The highest ablation rate of 50 mg/s was observed in Ref. 31 with a powder-filled anode, which is not considered here.

## III. VALIDATION OF THE ABLATION FLUX RELATION

Experimental data on the ablation rate as a function of the surface temperature are available in Ref. 8. The front surface of a cylindrical graphite target of a radius of 3 mm was heated up by a continuous wave laser in a helium atmosphere of 31 kPa (230 Torr). Various admixtures to the graphite were tried in Ref. 8 with virtually no effect on the ablation rate. The measurements were performed for temperatures up to 3600 K, which is lower than $T_{low}$ (3630 K for 31 kPa). Correspondingly, we should expect a low ablation regime in which the ablation rate is much lower than the one predicted by Langmuir's ablation formula (1), with a constant factor difference $\alpha_{diff}$, as given by Eq. (11). This is exactly what we see in Fig. 4, with a convenient choice of axes (natural logarithm of ablation rate and inversed temperature, similar to Ref. 8) that converts relations (1) and (11) into straight lines. Experimental points are lower than Langmuir's curve by a constant factor of $\alpha_{diff} = 0.01$.

A reduction factor $\alpha_{diff}$ of 0.01 corresponds to $d = 1$ mm, distance from the target front surface to a location where the carbon vapor condenses (see Fig. 2). This value agrees with the nanoparticle's detection results from Ref. 8: 1 mm is the closest distance to the ablating surface where carbon nanoparticles were detected indicating rapid condensation of carbon. This distance is also in good agreement with a temperature profile presented in Ref. 8 showing that at a distance 1 mm from the surface, temperature is reduced by 300 K which typically corresponds to rapid condensation of a vapor.[32]

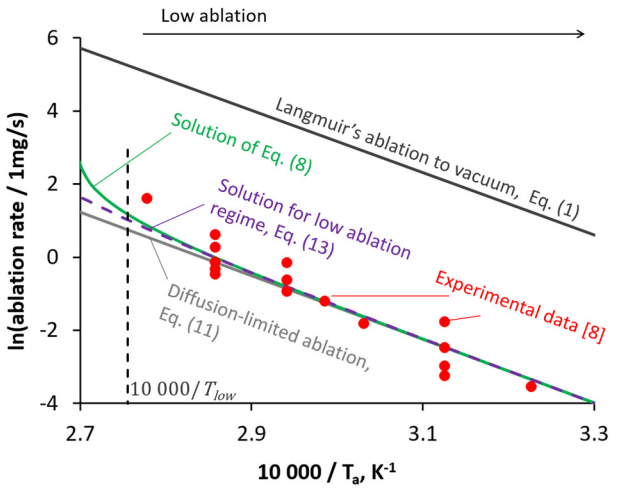


**FIG. 4.** Ablation rate vs inverse of the surface temperature $T_a$. Comparison between experimental data,[8] Langmuir's formula (1) for evaporation in vacuum, full solution (8), and approximate solutions (11), and (13) for the low ablation regime accounting for the ablation reduction by the background gas.

## IV. DETERMINING ANODE TEMPERATURE AND ABLATION RATE FROM THE ENERGY BALANCE

The ablation rate can be determined from the energy balance at the ablating surface in a carbon arc, i.e., the anode front surface, see Fig. 5. A sum of the heat sources at the surface must be equal to the sum of heat sinks. A list of the heat sinks and sources is provided below. Heat transfer through the anode body is considered in one-dimensional approximation valid for long cylindrical anodes typically used in arc experiments. The values of the model parameters are summarized in Appendix C. Additionally, in this section, remarks will be made on how this consideration can be applied to laser/solar ablation systems.

**Heat sinks at the anode front surface are as follows:**

(1) The heat sink corresponding to the ablation of the anode material is

$$\pi r_a^2 g_{abl} L,$$

where $r_a$ is the radius of the cylindrical anode and $L$ is the latent heat of graphite evaporation.

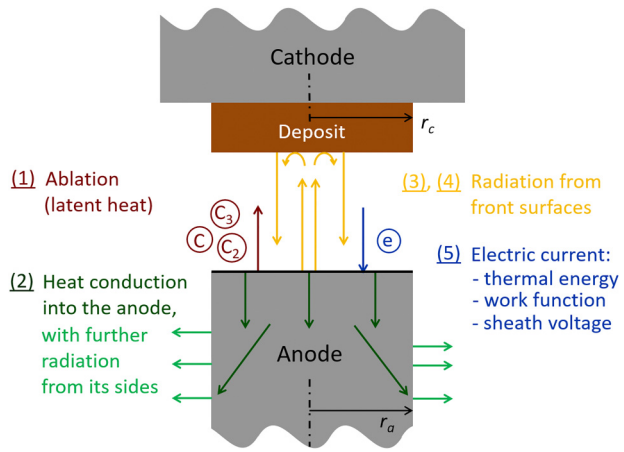


**FIG. 5.** Energy balance schematic at the anode front surface in a carbon arc. Equalizing the sum of heat sources at the surface to the sum of heat sinks yields the energy balance Eq. (14).

(2) The heat conduction into the anode body along the electrode's axis with further radiation from its side surface is given by[33]

$$\pi T_a^{2.5} r_a^{1.5} \sqrt{\frac{4}{5}\sigma\varepsilon_a\lambda_a},$$

where $T_a$ is the temperature of the anode front surface, $\sigma$ is the Stefan–Boltzmann radiation constant, $\lambda_a$ is the thermal conductivity of the anode (assumed constant along the electrode), and $\varepsilon_a$ is the emissivity of the anode surface.

This analytical expression for heat transfer in a long cylinder was obtained in Ref. 33, where it was also shown that the heat conduction to ambient gas and Joule heating in the electrode play a negligible role in determining heat flux through the anode front surface.

(3) The radiation energy loss from the front surface is given by

$$\pi r_a^2 \sigma\varepsilon_a T_a^4 (1-\alpha_r),$$

where $\alpha_r$ is a small coefficient accounting for the radiation reflected from the cathode front surface back to the anode (subsequent reflections between the anode and the cathode are neglected). It can be estimated as

$$\alpha_r = F_{a\to c}(1-\varepsilon_c)F_{c\to a}\varepsilon_a.$$

Here, $F_{a\to c}$ is a geometrical view factor between the cathode and anode front surfaces representing a fraction of radiation energy emitted from the anode front surface that reaches the cathode. Correspondingly, a product $F_{a\to c}(1-\varepsilon_c)$ represents a fraction of the anode emitted energy that is reflected back the cathode surface; $\varepsilon_c$ is the emissivity of the cathode surface. A product $F_{a\to c}(1-\varepsilon_c)F_{c\to a}$ represents a fraction of the emitted energy that is reflected from the cathode and reaches the anode. And, the full expression for the $\alpha_r$ represents a fraction of the emitted energy that is reflected back and is absorbed by the anode surface.

A view factor between two coaxial disks is given by[17,34]

$$F_{a\to c} = (x - \sqrt{x^2 - 4r_a^2/r_c^2})/2,$$

$$x = 1 + d^2/r_c^2 + r_a^2/r_c^2,$$

$$F_{c\to a} = F_{a\to c} r_a^2/r_c^2.$$

Here, $r_c$ is the radius of the cathode deposit that covers the cathode with a thick layer during the arc run and forms a new front surface reflecting and emitting radiation. This surface is also circular but narrower than the cathode. Experiments have shown that if a cathode is much wider than the anode, as it was in Refs. 16 and 17, with cathodes up to several centimeters wide, then the deposit is also considerably wide (see figures in these references) and view factor $F_{a\to c}$ is close to unity. For relatively narrow cathodes used in Refs. 1, 3, and 18 (diameter 9 mm), the cathode deposit is typically of the anode width ($r_c = r_a$). With a typical electrode separation $d = 1.5$ mm, the view factor is $F_{a\to c} = 0.6$.

Terms (1)–(3) are similar in the cases of electric arc and laser/solar ablation of a cylindrical target (as long as a target has a cylindrical shape, as in Refs. 7 and 8); $\alpha_r$ is zero in the light ablation cases.

**Heat sources at the anode front surface are as follows:**

(4) The thermal radiation from the cathode front surface reaching the anode. Making use of the relation for mutual view factors ratio,[34] $F_{c\to a} = F_{a\to c} r_a^2/r_c^2$, this heat source term can be written as

$$\pi r_a^2 \sigma\varepsilon_a(\varepsilon_c F_{a\to c} T_c^4).$$

Here, $T_C$ is the temperature of the cathode front surface equal to 3400 K to support thermionic emission.[24,30]

(5) Electrons bring thermal energy from the plasma, energy gained in the space-charge sheath and work function,[20,30,35–37]

$$\left(V_w + 2.5\frac{k}{e}T_{e,a} + \max(V_{sh}, 0)\right) I.$$

Here, $V_w$ is the work function of the anode material (4.6 eV for graphite), $T_{e,a}$ is the electron temperature in plasma at the anode surface, $V_{sh}$ is the voltage drop within the anode space-charge sheath, and $I$ is the arc current. The ion current at the anode surface is negligible,[33] hence, the electron current at the anode surface can be taken equal to the arc current.

As shown in Ref. 21 with 1D modeling of carbon arc accounting for ablation and chemical transformations in the gas phase, electron temperature near the anode surface $T_{e,a}$ is about 1.7 eV, very weakly dependent on the ablation rate and other arc parameters. The value is typically lower for arcs with no anode ablation.

Ablated carbon has to be ionized; carbon molecules need to be dissociated first. These processes require a lot of energy implying a high electric field near the anode and high electron temperature.

The anode sheath voltage in atmospheric pressure arcs is usually negative, of about 1–2 V.[20,38–40] However, when a surface of an electrode is hot, the electron emission can substantially change the sheath voltage and even inverse its sign.[41,42] As shown in Refs. 30 and 33, if the anode is hot (which is the case when graphite ablates), the anode sheath voltage $V_{sh}$ is positive to suppress the electron emission from its surface. The anode sheath voltage is proportional to the anode temperature and is roughly 0.5 V corresponding to the temperature of graphite ablation, $T_{sat}$.

With $V_w$, $T_{e,a}$, and $V_{sh}$ being almost constant, the electron heat flux expression can be simplified to

$$V_{eff} \times I,$$

with the effective voltage $V_{eff} = 9.5$ V.

The gas temperature gradient near the anode is small,[21,30,33] and the thermal conduction through the gas can be neglected.

For laser/solar ablation, terms (4) and (5) are irrelevant. In these cases, the heat source takes a simple form, $\varepsilon_a Q_{light}$, where $Q_{light}$ is the energy of the light beam to the target from the surface.

**Resultant energy balance equation:**

Equalizing the sum of heat sources at the front surface to the sum of heat sinks yields the following energy balance equation,

$$\pi r_a^2 g_{abl}(T_a)L + C_1 T_a^{2.5} r_a^{1.5} + C_2 r_a^2 T_a^4 = V_{eff}\, I + \ C_3 r_a^2. \tag{14}$$

Here, constants $C_1 = \pi\sqrt{\frac{4}{5}\sigma\varepsilon_a\lambda_a}$, $C_2 = \pi\sigma\varepsilon_a(1-\alpha_r)$, and $C_3 = \pi\sigma\varepsilon_a\varepsilon_c F_{c-a} T_c^4$ originate the terms accounting for the heat conduction through the anode body, radiation from the anode front surface, and incident radiation from the cathode, respectively. These values are summarized in Appendix C.

Equations (13) and (8) represent a system with two unknowns: the surface temperature $T_a$ and the ablation flux $g_{abl}$. The ablation rate is equal to the ablation flux times anode front surface area: $G_{abl} = \pi r_a^2 g_{abl}$. An exact solution can be obtained numerically. Alternatively, the arc current $I$ can be obtained directly as a function of the ablation rate by substituting the surface temperature obtained from (9) into (14). In the next section, we derive analytical solutions.

The values of the model parameters are summarized in Appendix C. Note that the model parameters that depend on the arc plasma (the electron temperature, cathode temperature, ion current, and sheath voltage) are almost constant or small compared to the work function term. It allows excluding the arc plasma from the ablation model making it simple.

## V. ARC ABLATION RATE RELATIONS FOR LOW AND HIGH ABLATION REGIMES

### A. Low ablation regime

In a low ablation regime, for temperatures below $T_{low}$ defined in Eq. (12), the ablation rate term plays a minor role in the heat balance equation (14). Other terms in Eq. (14) are relatively weak functions of the surface temperature $T_a$, hence, Eq. (14) can be linearized in the vicinity of $T_{low}$ to express $T_a$,

$$T_a = V_{eff} I/A + B, \tag{15}$$

where

$$A = 2.5C_1 T_{low}^{1.5} r_a^{1.5} + 4C_2 r_a^2 T_{low}^3 + \pi r_a^2 g'(T_{low})L$$
$$B = T_{low} - (C_1 T_{low}^{2.5} r_a^{1.5} + C_2 r_a^2 T_{low}^4 + \pi r_a^2 g_0 L)/A,$$

where $g_0$ is the ablation flux at $T_a = T_{low}$ given by Eq. (7), $g'(T_{low})$ is a derivative of ablation flux given by Eq. (10) at $T_a = T_{low}$,

$$g'(T_{low}) = \frac{g_0}{T_{low}}\left(\frac{Lm}{kT_{low}} - 1\right).$$

For the evaporation of carbon at the background pressure of 67 kPa (500 Torr), $g'(T_{low}) \approx 2.2 g_0/T_{low}$. The ablation rate can be obtained by substituting $T_a$ from (15) into (13),

$$G_{abl} = \pi r_a^2 g_0 \left[\frac{p_0}{p}\exp\left(-\frac{Lm}{k(V_{eff} I/A + B)}\right) + \frac{1}{2}\left(\frac{p_0}{p}\exp\left(-\frac{Lm}{k(V_{eff} I/A + B)}\right)\right)^2\right]. \tag{16}$$

This solution holds for the anode surface temperature $T_a$ below $T_{low}$ and, correspondingly, ablation flux below $g_0$. At $T_a = T_{low}$ and $g_{abl} = g_0$, Eq. (14) transforms to the following relation between the anode radius and the arc current:

$$r_a^2[\pi L g_0 + C_1 T_{low}^{2.5} r_a^{-0.5} + C_2 T_{low}^4 - C_3] = V_{eff} I. \tag{17}$$

A transition to the high ablation regime begins when the arc current becomes higher than one predicted by Eq. (17) (if the anode radius is fixed), or when the anode radius becomes smaller than one predicted by Eq. (17) (if the arc current is fixed).

### B. High ablation regime

In the high ablation regime, the ablation rate grows drastically (several orders of magnitude) while the surface temperature $T_a$ is almost constant, close to the carbon vapor saturation temperature $T_{sat}$, see Fig. 3. Consequently, the ablation rate in this regime can be determined by substituting $T_{sat}$ into Eq. (14),

$$G_{abl} = (V_{eff} I + \ C_3 r_a^2 - C_1 T_{sat}^{2.5} r_a^{1.5} - C_2 r_a^2 T_{sat}^4)/L. \tag{18}$$

Note that the ablation rate in this regime does not depend on the diffusion characteristics, i.e., parameter $g_0$. It is solely determined by the heat balance and the saturation temperature $T_{sat}$ which depends on the background pressure $p$ [see Eq. (4)].

## VI. RESULTS AND DISCUSSION

Multiple experiments have been conducted with carbon arcs for nano-synthesis.[4,16–18] In these experiments, arcs were run between two long cylindrical electrodes in an atmosphere of helium

at $p = 67$ kPa. Each experimental run was performed at constant arc parameters for a sufficiently long time to consider the arc established so that the parameters do not vary with time. Electrode separation was kept constant by automatically adjusting electrode's positions to compensate for the ablation of a graphite anode ablation and growth of a deposit on a cathode. The ablation rate was accurately measured by weighting the electrodes before and after the experiments. The ablation rate data were collected for various radii of electrodes, their separation distances, and electric currents. These data allow a comprehensive validation of the ablation model.

### A. Comparison of analytical formulas for the ablation rate to published experimental data

In experiments,[18] arc current was varied, whereas other arc parameters were kept unchanged. The anode radius was $r_a = 3$ mm. Electrode separation $d$ was maintained in a range of 1 mm–2 mm (we use average value $d = 1.5$ mm in the model). Cathodes of 4.5 mm in radius were used, on top of which a deposit of a radius $r_c = 3$ mm formed (see Fig. 7 in Ref. 18 and Fig. 2 in Ref. 1 for a similar arc) corresponding to a view factor between the cathode and the anode $F_{a\to c} = 0.6$.

Experimental data are compared to modeling results in Fig. 6. As evident from the figure, modeling results given by a numerical solution of Eqs. (8) and (14) are in good agreement with the experimental data. A sharp transition between low and high ablation regimes observed in the experiment is well captured by the modeling. Analytical solutions for low and high ablation regimes given by Eqs. (16) and (18) are in good agreement with both the numerical solution (at corresponding parts of the curve) and the experimental data. The analytical solutions for two regimes cover a substantial part of the curve and generally allow reconstructing the ablation rate behavior without the need for numerical tools.

The analytical solution for the low ablation regime given by Eq. (16) was plotted for the surface temperatures $T_a \le T_{low}$, with $T_{low} = 3760$ K [as defined in Eq. (12)] corresponding to the arc current defined by Eq. (17) determining the right end of the dashed blue curve in Fig. 6. In the low ablation regime, the ablation rate is substantially reduced by the ambient helium; its dependence on $T_a$ and the arc current is exponential, but the values are low. Most of the anode heating is radiated away from its surfaces, the ablation rate is a minor fraction of the anode energy balance.

With the arc current increase, when the temperate of the anode front surface $T_a$ approaches the carbon vapor saturation temperature $T_{sat} = 3830$ K, then the ablation rate becomes incredibly sensitive to $T_a$ (see Fig. 3). Further increase of the arc current and corresponding increase of the anode heating has very little effect on the front surface temperature. The radiation and heat conduction terms do not change, and all the additional heat goes to the ablation rate increase. The ablation rate is well described by the analytical solution (18) which takes a form of a straight line with a slope $V_{eff}/L$.

To study the effect of the background pressure $p$ on the ablation rate, calculations were performed for various background pressures while other conditions were the same as in the experiments.[18] The results are plotted in Fig. 7 as functions of the arc current. As expected from Eq. (18), straight parts of the curves corresponding to the high ablation regime shift to the right (to higher arc currents) with the background pressure increase. In the high ablation regime, the surface temperature is equal to the saturation temperature $T_{sat}$, which is a logarithmic function of the background pressure. $T_{sat}$ grows with the background pressure thereby increasing

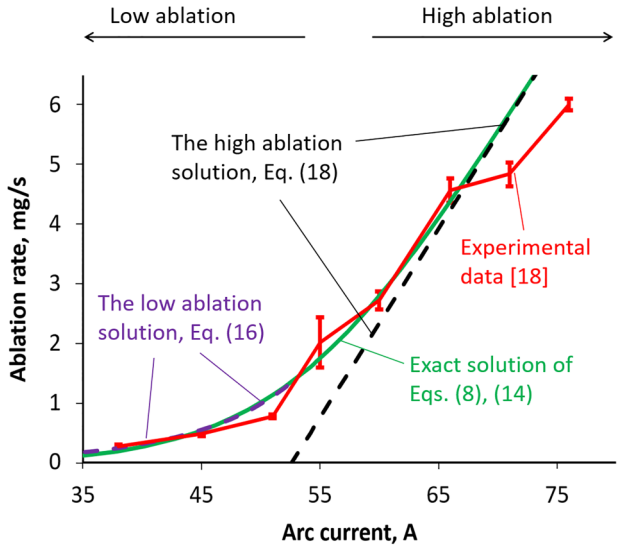


**FIG. 6.** Ablation rate as a function of arc current for fixed inter-electrode gap width d = 1.5 mm and anode radius $r_a$ = 3 mm. Good agreement between the numerical solution of Eqs. (8) and (14), analytical solutions for low and high ablation regimes [Eqs. (16) and (18)] and experimental data[18] is obtained.

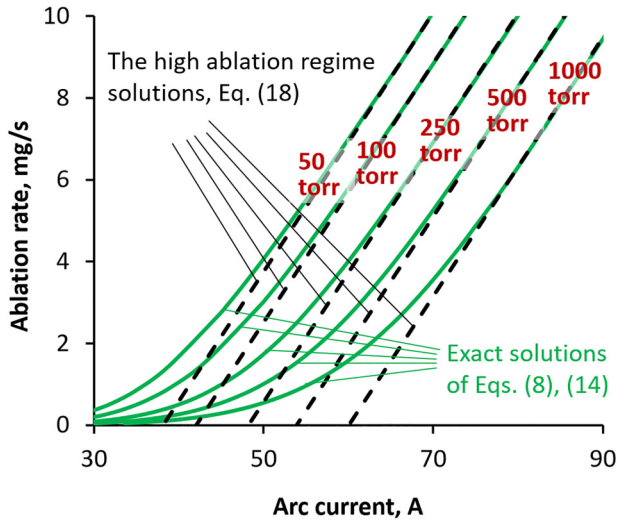


**FIG. 7.** Ablation rate as a function of arc current for variable background pressure p and fixed inter-electrode gap width d = 1.5 mm and anode radius $r_a$ = 3 mm.

radiative and thermal energy losses from the anode and leaving less heat for the ablation. Generally, at any arc current, the ablation rate decreases with the background pressure.

In the experiments from Refs. 16 and 17, the anode radius was varied, while the arc current and inter-electrode gap were constant, 65 A and 1.5 mm, respectively. The experimental data and modeling results are plotted in Fig. 8. The analytical solution for the low ablation regime given by Eq. (16) was plotted for the surface temperatures $T_a \leq T_{low}$ correspond to the anode radii above 3.8 mm as predicted by Eq. (17).

As one can notice, experimental data from different sources slightly vary. This can be explained by measurement errors and some differences in experimental setups. For example, in Ref. 18, relatively narrow cathodes were used, deposit radius was $r_c = 3$ mm corresponding to view factor $F_{a\to c} = 0.6$. In Refs. 16 and 17, cathodes of radii 6 mm and 25 mm were used growing a much wider deposit on them (see Fig. 3 in Ref. 17) corresponding to a view factor of about $F_{a\to c} \approx 1$. A higher view factor implies higher radiation energy flux from the cathode to the anode and higher ablation rate. Unity value was used in the model in this case.

As evident from Fig. 8, the numerical solution of Eqs. (8) and (14) is in good agreement with the experimental data for a low ablation regime. For the high ablation regime, the modeling results lie within the uncertainty range of the experimental data. The abrupt transition between high and low ablation regimes is well captured by the model.

When the anode is wide, energy losses due to radiation from its surface are high and the ablation rate is low. The narrower the anode, the lower are the radiation losses, the higher is the surface temperature $T_a$ and the higher is the ablation rate. When $T_a$ approaches $T_{sat}$, its variation is diminished due to very high influence on the ablation rate, and the system goes to the high ablation regime described by Eq. (18).

### B. Comparison of the analytical formula for the ablation rate to in-house experimental data

In our arc experiments previously reported in Ref. 26, the inter-electrode gap was varied for the constant arc current of 60 A and anode radius of $r_a = 3$ mm. The cathode radius was 4.5 mm corresponding to the deposit radius $r_c = 3$ mm. The experimental data are presented in Fig. 9 in comparison with the modeling results and the analytical solution for high ablation regime. Good agreement between the analytical solutions and the experimental data is observed.

As evident from the figure, the inter-electrode gap width noticeably affects the ablation rate: with the gap variation from 0.5 mm to 3 mm the ablation rate changes by a factor of 2.5. The lower is the distance between the electrodes, the higher is the ablation rate. Numerical simulations of carbon arc discharges at similar conditions[24] showed that the near-anode layer in plasma is quite narrow, considerably smaller than 0.5 mm. Therefore, if the gap width is kept above 0.5 mm, its variation should affect neither plasma parameters in the vicinity of the anode nor the heat flux from the plasma to the anode which can be determined as $V_{eff} \times I$. The solutions plotted in Fig. 9 show that the arc is operating in a nearly high ablation regime in which the ablation rate does not depend on the carbon diffusion process but solely depends on the anode heat balance. The parameter that affects the anode energy balance and depends on the gap width is the radiation view factor $F_{a\to c}$: $F_{a\to c} = 0.38$ for $d = 3$ mm; $F_{a\to c} = 0.85$ for $d = 1$ mm. Our modeling shows that the variation of the ablation rate can be explained by the radiation view factor. The narrower the gap, the higher fraction of cathode thermal radiation reaches the anode, and the higher is the ablation rate.

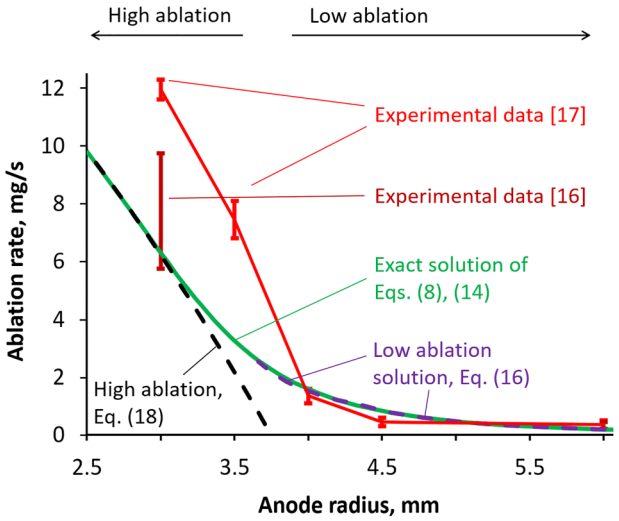


**FIG. 8.** Ablation rate as a function of the anode radius $r_a$ for arc current I = 65 A and inter-electrode gap d = 1.5 mm. Good agreement between the numerical solution of Eqs. (8) and (14), analytical solutions for low (16) and high (18) ablation regimes and experimental data is obtained.

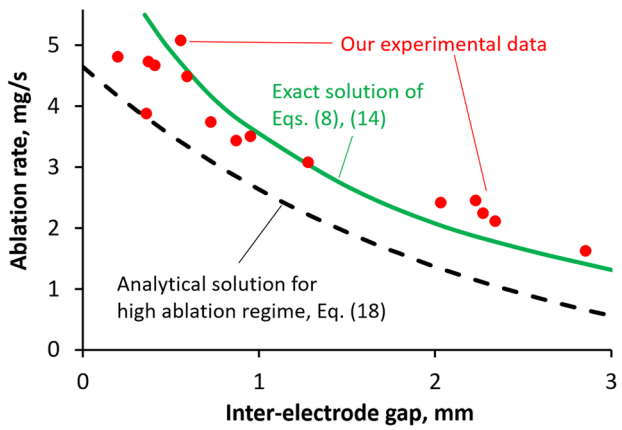


**FIG. 9.** Ablation rate as a function of the electrode separation distance d for the arc current I = 60 A and anode radius $r_a$ = 3 mm. Good agreement between the numerical solution of Eqs. (8) and (14), analytical solution (18) for high ablation regime and experimental data is obtained.

## VII. SUMMARY

A model predicting the ablation rate of a heated graphite surface into a background gas was developed, Eqs. (8) and (14), and thoroughly validated by comparison to multiple experimental data for carbon arcs and a laser ablation system. Good agreement between the model and the experimental data was obtained. The manifestation of distinct high and low ablation regimes observed in the arc experiments was explained. A rapid transition between the ablation regimes was well captured by the model. Convenient analytical expressions for the ablation rate in different ablation regimes were derived. The effect of the background pressure on the ablation rate was studied.

It was shown that the presence of the background gas drastically affects the ablation rate and plays a crucial role in the formation of distinct ablation regimes. It causes an accumulation of the ablated material (i.e., carbon vapor) near the ablation surface and its deposition back to the surface.

At a low surface heating (i.e., at a low arc current or in the case of a wide anode), when the anode surface temperature is below the carbon vapor saturation temperature $T_{sat}$ [Eq. (4)], the flow of the ablated material away from the ablating surface is strongly impeded by the background gas. The carbon vapor is almost at equilibrium with the surface, i.e., the ablation and deposition fluxes almost cancel out each other. The net ablation flux is proportional to the saturation pressure (as would be in the case of evaporation into vacuum), but with a small coefficient, Eq. (11). This is the low ablation regime. The anode ablation rate is approximated by Eq. (16).

In the case of a high surface heating (i.e., at a high arc current or in the case of a narrow anode), when the surface temperature is higher than the saturation temperature, the carbon vapor pressure is limited by the background pressure. The ablation rate changes drastically with a small variation of the surface temperature. Accordingly, the surface temperature is equal to $T_{sat}$ and virtually does not depend on the surface heating rate. This is the high ablation regime. The anode ablation rate is approximated by Eq. (18).

With the background pressure increase, the ablation rate decreases, and a transition to the high ablation regime occurs at a higher arc current.

## ACKNOWLEDGMENTS

The authors would like to thank Dr. Valerian Nemchinsky (Keiser University, FL), Dr. Yevgeny Raitses (PPPL), and Jian Chen (PPPL) for fruitful discussions. The theoretical work was supported by the U.S. Department of Energy (DOE), Office of Science, Fusion Energy Sciences. The arc experiments were supported by the U.S. DOE, Office of Science, Basic Energy Sciences, Materials Sciences and Engineering Division.

## APPENDIX A: PARAMETERS FOR THE GRAPHITE ABLATION FLUX

The ablation flux relations (1) and (3) are formulated for single gas species. However, several carbon species ablate from a surface of graphite: atoms C and molecules $C_2$ and $C_3$, as predicted by thermodynamic modeling[1,43,44] and observed in experiments.[1,43,45] A detailed model of the ablation process would require separate consideration of species C, $C_2$, and $C_3$ (as done in Ref. 21) with individual ablation rates. Luckily, the value of the latent heat per one particle ($L \times m$) in the exponent of saturation pressure expression (2) is close for C, $C_2$, and $C_3$ (see Refs. 21 and 45–48), and mass of ablating particles is under a radical in thermal velocity expression. This allows a rather accurate determination of total ablation flux with a single relation (3). Following values of the material parameters were used in the present model: $L \cdot m_C = 1.2 \times 10^{-18}$ J, $p_0 = 4.8 \times 10^{14}$ Pa (corresponding to $p_{sat,C}$ equal to 1 atm at 3900 K), $m_C = 4.0 \times 10^{-26}$ kg (corresponding to the mass of a $C_2$ molecule).

## APPENDIX B: DIFFUSION EQUATION FOR THE TRANSPORT OF CARBON GAS

Even though not only carbon atom atoms but also carbon molecules $C_2$ and $C_3$ ablate from a graphite surface (as discussed in Appendix A), the molecules are only present in very thin regions near the arc electrodes where the temperature is low[43] and, therefore, do not play important role in the carbon transport in the arc volume (from the anode toward the cathode). The same can be said for the carbon transport in a laser ablation system,[7,8] where carbon molecules $C_2$ and $C_3$ were only detected at a distance of about 1 mm from the ablating surface where carbon condenses and nanoparticles form. Thereby, diffusion of carbon atoms only is considered here.

Diffusion of carbon atoms through other components of a carbon arc or a light beam ablation plasma is accurately described by the Stefan–Maxwell equation[27–30] derived from the kinetic theory of gases. In a one-dimensional form, this equation reads

$$\sum_j \frac{n_C n_j k T C_{C-j}}{n D_{C-j}} (v_C - v_j) = -\frac{dp_C}{dx} + Y_C \frac{dp}{dx} - C_C^{(e)} n_C k \frac{dT}{dx}. \quad \text{(B1)}$$

Here, index $j$ denotes a gas mixture component other than carbon atoms [helium atoms (He), carbon ions (i), and electrons (e)], $x$ is a coordinate in a direction perpendicular to the ablating surface, $p$ is the mixture pressure, $T$ is the temperature (assumed equal for all species), $p_C = n_C k T$ is the partial pressure of carbon gas, $k$ is the Boltzmann constant, $Y_C$ is the mass fraction of carbon atoms, $v_i$ are individual mass-averaged velocities of different species, $n_i$ are species densities, $C_{C-j}$ and $C_C^{(e)}$ are kinetic coefficients, and $D_{C-j}$ are binary diffusion coefficients given by

$$n D_{C-i} = \frac{3\pi}{32} \sqrt{\frac{8kT}{\pi m_{C-j}}} \frac{1}{\sigma_{C-j}}, \quad m_{C-j} = \frac{m_{C,a} m_j}{m_{C,a} + m_j}, \quad \text{(B2)}$$

where $\sigma_{C-j}$ is a collision cross section of carbon atoms with species $j$; $m_{C,a}$ is the mass of carbon atoms; $m_j$ are other species masses, and $n = \sum n_i = p/kT$ is the gas mixture density.

In general, Eq. (B1) describes the momentum balance for carbon atoms: friction of carbon atoms with other mixture species due to their relative motion is compensated by the gradients of the species pressures and temperatures. Equation (B1) has a complex form; however, only two of its terms are large, the rest can be neglected as discussed below.

Kinetic coefficient $C_C^{(e)}$ is of an order of the ionization degree,[28,30] which is typically below 0.1 in a carbon arc,[24] hence, the last term in Eq. (B1) is small in comparison to the first term in the right-hand side (RHS) of Eq. (B1) and can be neglected.

The variation of the carbon atoms partial pressure $p_C$ is by many orders of magnitude higher than the variation of the mixture pressure $p$. $p_C$ varies from its maximum at the ablating surface, where it is comparable to $p$ to almost zero at the region where carbon condensation happens (a cathode surface in a carbon arc or a volumetric condensation region in the case of a light beam ablation, see Fig. 2). From the Bernoulli equation, the variation of the mixture pressure $p$ is of an order of $\rho v^2$ or $g^2/\rho$, where $\rho$ is the mixture density ($\approx$0.02kg/m$^3$ for carbon gas at 67 kPa and 5000 K typical for carbon arc[24]), $v$ is the mass-averaged flow velocity and $g$ is the ablation flux [below 0.3 kg/(m$^2$ s) corresponding to 10 mg/s from a 3 mm radius surface, as in the arc and light-beam ablation experiments]. With these parameters, the variation of the mixture pressure $p$ is about 5 Pa, much lower than $p$ itself (67 kPa) and the variation of $p_C$. With this said, the second term in the RHS of Eq. (B1) can be neglected.

For convenience, the left-hand side (LHS) of Eq. (B1) can be reformulated in terms of particle fluxes,

$$\sum_j \frac{C_{C-j}}{nD_{C-j}}(p_j J_C - p_C J_j) = -\frac{dp_C}{dx}. \tag{B3}$$

Here, $J_j = n_j v_j = g_j/m_j$ is the particle flux of species $j$, $p_j = n_j kT$ is the species partial pressure. With three mixture species $j$ other than carbon atoms [helium atoms (He), carbon ions (i), and electrons (e)], there are six terms in the LHS of Eq. (B2). However, among these terms only the one with $p_{He}J_C$ is important; other terms are small and can be neglected, as is shown below.

Collision cross sections between the species are $\sigma_{C-He} \approx 3\times10^{-19}$ m$^2$,[49] $\sigma_{C-e} \approx 2\times10^{-19}$ m$^2$[50,51] (for low-energy elastic collisions), $\sigma_{C-i} \approx 7\times10^{-19}$ m$^2$[52,53] (charge exchange cross section for the carbon atom-ion collisions). The binary masses are $m_{C-He} = 1.5\times10^{-26}$ kg, $m_{C-e} = 9\times10^{-31}$ kg, $m_{C-i} = 10^{-26}$ kg. Binary diffusion coefficients between carbon atoms and other species, as defined by (B2), are weak functions of temperature. For typical temperature in electric arc, 5000 K, the diffusion coefficients are equal to $nD_{C-He} = 5\times10^{21}$ m$^{-1}$s$^{-1}$, $nD_{C-i} = 2\times10^{21}$ m$^{-1}$s$^{-1}$, $nD_{C-e} = 10^{24}$ m$^{-1}$s$^{-1}$.

For a typical carbon arc with a current of 70 A, ablation rate 3 mg/s, and anode radius 3 mm, particle fluxes of carbon atoms and electrons, correspondingly, are $J_C = 5\times10^{24}$ m$^{-2}$s$^{-1}$, $J_e = 1.5\times10^{25}$ m$^{-2}$s$^{-1}$. Ion flux can be estimated as $J_i \approx J_e\sqrt{m_e/m_C} = 10^{23}$ m$^{-2}$s$^{-1}$. In light-beam ablation systems, ion and electron fluxes are negligible. The background gas, i.e., helium, is not moving, hence $J_{He} = 0$.

Partial pressures of carbon $p_C$ and helium $p_{He}$ are of the same order, partial pressures of ions $p_i$ and electrons $p_e$ are by more than an order of magnitude lower, corresponding to the ionization degree below 0.1.[24]

Kinetic coefficients $C_{C-j}$ are of an order of unity;[28,30] $C_{C-He} = 1$.

With the above-written estimates, ratios of the terms in the LHS of (B3) can be determined,

$$\frac{p_{He}J_C}{nD_{C-He}} \Big/ \frac{p_C J_{He}}{nD_{C-He}} \Big/ \frac{p_i J_C}{nD_{C-i}} \Big/ \frac{p_C J_i}{nD_{C-i}} \Big/ \frac{p_e J_C}{nD_{C-e}} \Big/ \frac{p_C J_e}{nD_{C-e}}$$
$$\approx 1/0/0.01/0.03/3\times10^{-5}/0.01. \tag{B4}$$

As evident from relation (B4), all terms in the LHS of (B3) except for the term containing $p_{He}J_C$ are small and can be neglected, thereby reducing (B3) to

$$\frac{p_{He}}{nD_{C-He}} J_C = -\frac{dp_C}{dx}, \tag{B5}$$

where $J_C = g_C/m_{C,a}$. In a one-dimensional consideration, carbon flux $g_C$ is constant (does not vary with $x$) equal to the ablation flux $g_{abl}$. According to Eq. (B5), the major mechanism for the carbon gas motion is its diffusion through stationary helium driven by the carbon gas pressure gradient.

Since the variation of the gas mixture pressure $p$ is small and the fraction of electrons and ions in the gas mixture is low, the sum of carbon and helium partial pressures can be taken constant, equal to the background pressure,

$$p_C + p_{He} \approx p = const. \tag{B6}$$

Using (B6), $p_{He}$ can be excluded from Eq. (B5),

$$\frac{p - p_c}{nD_{c-He}} \frac{g_{abl}}{m_{c,a}} = -\frac{dp_c}{dx}. \tag{B7}$$

Equation (B7) can be solved analytically for $p_C$,

$$p_C = p - C\,exp\left(-\frac{x}{nD_{C-He}}\frac{g_{abl}}{m_{C,a}}\right), \tag{B8}$$

where $x$ is the distance from the ablation surface, and $C$ is a constant determined from the boundary conditions. Zero carbon density can be used as a boundary condition at a location $x = d$ corresponding to either a cathode surface in an electric arc or a condensation layer in the laser/solar ablation case, see Fig. 2. With this, the constant $C$ can be determined yielding the following carbon density profile:

$$p_C = p - p\exp\left(\frac{d-x}{nD_{C-He}}\frac{g_{abl}}{m_{C,a}}\right). \tag{B9}$$

Substituting $x = 0$ into (B9) yields carbon density at the ablation surface, $p_{C,a}$,

$$p_{C,a} = p\left[1 - \exp\left(-\frac{g_{abl}}{g_0}\right)\right], \tag{B10}$$

where $g_0 = \frac{m_{C,a}nD_{C-He}}{d}$.

**TABLE I.** Values of the parameters used in the model.

| Parameter | Value | Reference |
|---|---|---|
| $L$ | $3 \times 10^7$ J/kg | 45–48 |
| $L \cdot m_C$ | $1.2 \times 10^{-18}$ J | |
| $p_0$ | $4.8 \times 10^{14}$ Pa | |
| $\varepsilon_a = \varepsilon_c$ | 0.8[a] | 1 and 54 |
| $T_c$ | 3400 K[b] | 30 |
| $\lambda_a$ | 14 W/m/K[c] | 17 and 55 |
| $V_{eff}$ | 9.5 V | |
| $m_C$ | $4.0 \times 10^{-26}$ kg | Mass of a $C_2$ molecule |
| $m_{C,a}$ | $2.0 \times 10^{-26}$ kg | Mass of a carbon atom |
| $m_{C-He}$ | $5.0 \times 10^{-27}$ kg | Binary mass of a carbon and helium atoms |
| $\sigma_{C-He}$ | $3 \times 10^{-19}$ m$^2$ | 49 |
| $nD_{C-He}$ | $5 \times 10^{21}$ m$^{-1}$s$^{-1}$ | 49 |
| $F_{a\to c}$ | = 0.6 for a narrow cathode ($r_c = 4.5$ mm) and $d = 1.5$ mm as in Ref. 18; see Ref. 34<br>= 1 for a wide cathode as in Refs. 16 and 17 | |
| $\alpha_r$ | = 0.06 for a narrow cathode, as in Ref. 34;<br>= 0.16 for a wide cathode, as in Refs. 16 and 17 | |
| $C_1$ | 0.00225 W K$^{-2.5}$ m$^{-1.5}$ | |
| $C_2$ | $= 1.35 \times 10^{-7}$ W K$^{-4}$ m$^{-2}$ for a narrow cathode, as in Ref. 34;<br>$= 1.2 \times 10^{-7}$ W K$^{-4}$ m$^{-2}$ for a wide cathode, as in Refs. 16 and 17 | |
| $C_3$ | $=9.3 \times 10^6$ W m$^{-2}$ for a narrow cathode, as in Ref. 34;<br>$=1.5 \times 10^7$ W m$^{-2}$ for a wide cathode, as in Refs. 16 and 17 | |
| $T_{low}$ | 3750 K at 67 kPa (500 Torr); 3630 K at 31 kPa (230 Torr) | |
| $T_{sat}$ | 3830 K at 67 kPa (500 Torr); 3700 K at 31 kPa (230 Torr) | |

[a]This value is used for both the anode graphite and the cathode deposit.[17,54]

[b]Cathode temperature is very weakly (logarithmically) dependent on the arc current;[24,30] a constant value of 3400 K is used in the model.

[c]The value for a graphite at a high temperature is taken, corresponding to a region near the front surface where a major part of the heat transfer takes place.

## APPENDIX C: VALUES OF THE MODEL PARAMETERS

Values of the parameters used in the model are summarized in Table I.

## DATA AVAILABILITY

The data that support the findings of this study are available from the corresponding author upon reasonable request.

## REFERENCES


[1]S. Yatom, A. Khrabry, J. Mitrani, A. Khodak, I. Kaganovich, V. Vekselman, B. Stratton, and Y. Raitses, "Synthesis of nanoparticles in carbon arc: Measurements and modeling," MRS Commun. **8**, 842–849 (2018).

[2]M. Kundrapu and M. Keidar, "Numerical simulation of carbon arc discharge for nanoparticle synthesis," Phys. Plasmas **19**, 073510 (2012).

[3]S. Yatom, R. S. Selinsky, B. E. Koel, and Y. Raitses, "'Synthesis-on' and 'synthesis-off' modes of carbon arc operation during synthesis of carbon nanotubes," Carbon **125**, 336–343 (2017).

[4]J. Fetterman, Y. Raitses, and M. Keidar, "Enhanced ablation of small anodes in a carbon nanotube arc plasma," Carbon **46**, 1322 (2008).

[5]A. Szabó, C. Perri, A. Csató, G. Giordano, D. Vuono, and J. B. Nagy, "Synthesis methods of carbon nanotubes and related materials," Materials **3**, 3092–3140 (2010).

[6]S. Arepalli, "Laser ablation process for single-walled carbon nanotube production," J. Nanosci. Nanotechnol. **4**, 317–325 (2004).

[7]M. Cau, N. Dorval, B. Cao, B. Attal-Trétout, L. Cochon, A. Loiseau, S. Farhat, and C. D. Scott, "Spatial evolutions of Co and Ni atoms during single-walled carbon nanotubes formation: Measurements and modeling," J. Nanosci. Nanotechnol. **6**, 1298–1308 (2006).

[8]M. Cau, N. Dorval, B. Attal-Trétout, J.-L. Cochon, A. Foutel-Richard, A. Loiseau, V. Krüger, M. Tsurikov, and C. D. Scott, "Formation of carbon nanotubes: *In situ* optical analysis using laser-induced incandescence and laser-induced fluorescence," Phys. Rev. B **81**, 165416 (2010).

[9]D. Laplaze, L. Alvarez, T. Guillard, J. M. Badie, and G. Flamant, "Carbon nanotubes: Dynamics of synthesis processes," Carbon **40**, 1621 (2002).

[10]R. Das, Z. Shahnavaz, E. Ali, M. M. Islam, and S. B. A. Hamid, "Can we optimize arc discharge and laser ablation for well-controlled carbon nanotube synthesis?," Nanoscale Res. Lett. **11**, 510 (2016).

[11]X. Q. Fang, A. Shashurin, G. Teel, and M. Keidar, "Determining synthesis region of the single wall carbon nanotubes in arc plasma volume," Carbon **107**, 273 (2016).

[12]T. Guillard, S. Cetout, G. Flamant, and D. Laplaze, "Solar production of carbon nanotubes; structure evolution with experimental conditions," J. Mater. Sci. **35**, 419–425 (2000).

[13]K. Ostrikov and A. B. Murphy, "Plasma-aided nanofabrication: Where is the cutting edge?," J. Phys. D Appl. Phys. **40**, 2223 (2007).

[14]M. Keidar, A. Shashurin, J. Li, O. Volotskova, M. Kundrapu, and T. S. Zhuang, "Arc plasma synthesis of carbon nanostructures: Where is the frontier?," J. Phys. D Appl. Phys. **44**, 174006 (2011).

[15]M. Meyyappan, *Carbon Nanotubes: Science and Applications* (CRC, Boca Raton, 2004).

[16]J. Ng and Y. Raitses, "Role of the cathode deposit in the carbon arc for the synthesis of nanomaterials," Carbon **77**, 80 (2014).

[17]J. Ng and Y. Raitses, "Self-organisation processes in the carbon arc for nano-synthesis," J. Appl. Phys. **117**, 063303 (2015).

[18]V. Vekselman, M. Feurer, T. Huang, B. Stratton, and Y. Raitses, "Complex structure of the carbon arc discharge for synthesis of nanotubes," Plasma Sources Sci. Technol. **26**, 065019 (2017).

[19]V. Nemchinsky and Y. Raitses, "Atmospheric pressure arc discharge with ablating graphite anode," J. Phys. D Appl. Phys. **48**, 245202 (2015).

[20]V. Nemchinsky and Y. Raitses, "Anode sheath transition in an anodic arc for synthesis of nanomaterials," Plasma Sources Sci. Technol. **25**, 035003 (2016).

[21]A. R. Mansour and K. Hara, "Multispecies plasma fluid simulation for carbon arc discharge," J. Phys. D Appl. Phys. **52**, 105204 (2019).

[22]I. Langmuir, "The vapor pressure of metallic tungsten," Phys. Rev. **2**, 329 (1913).

[23]M. S. Benilov, S. Jacobsson, A. Kaddani, and S. Zahrai, "Vaporization of a solid surface in an ambient gas," J. Phys. D Appl. Phys. **34**, 1993–1999 (2001).

[24]J. Chen, A. Khrabry, I. D. Kaganovich, A. Khodak, V. Vekselman, and H.-P. Li, "Validated two-dimensional modeling of short carbon arcs: Anode and cathode spots," Phys. Plasmas **27**, 083511 (2020).

[25]J. Huo, J. Ronzello, A. Rontey, Y. Wang, L. Jacobs, T. Sommerer, and Y. Cao, "Development of an arc root model for studying the electrode vaporization and its influence on arc dynamics," AIP Adv. **10**, 085324 (2020).

[26]A. Khrabry, I. D. Kaganovich, A. Khodak, V. Vekselman, and Y. Raitses, "Validated modeling of atmospheric-pressure anodic arc," arxiv.org/abs/1902.09991 (2019).

[27]J. O. Hirschfelder, C. F. Curtiss, and R. B. Bird, *Molecular Theory of Gases and Liquids* (Wiley, New York, 1964), p. 1219.
[28]N. A. Almeida, M. S. Benilov, and G. V. Naidis, "Unified modelling of near-cathode plasma layers in high-pressure arc discharges," J. Phys. D Appl. Phys. **41**, 245201 (2008).
[29]M. Baeva, M. S. Benilov, N. A. Almeida, and D. Uhrlandt, "Novel non-equilibrium modelling of a DC electric arc in argon," J. Phys. D Appl. Phys. **49**, 245205 (2016).
[30]A. Khrabry, I. D. Kaganovich, V. Nemchinsky, and A. Khodak, "Investigation of the short argon arc with hot anode. I. numerical simulations of non-equilibrium effects in the near-electrode regions," Phys. Plasmas **25**, 013521 (2018).
[31]A. Shashurin, M. Keidar, and I. I. Beilis, "Voltage-current characteristics of an anodic arc producing carbon nanotubes," J. Appl. Phys. **104**, 063311 (2008).
[32]M. Tacu, A. Khrabry, and I. D. Kaganovich, "Analytical formula for cluster diameter and its dispersion at the end of nucleation stage," Phys. Rev. E, arxiv.org/pdf/1903.12268.pdf (2019), submitted.
[33]A. Khrabry, I. D. Kaganovich, V. Nemchinsky, and A. Khodak, "Investigation of the short argon arc with hot anode. II. Analytical model," Phys. Plasmas **25**, 013522 (2018).
[34]D. C. Hamilton and W. R. Morgan, "Radiant-interchange configuration factors," NACA-TN-2836 (1952), https://archive.org/details/nasa_techdoc_19930083529/page/n1.
[35]M. Baeva, "Non-equilibrium modeling of tungsten-inert gas arcs," Plasma Chem. Plasma Process. **37**, 341–370 (2017).
[36]L. Pekker and N. Hussary, "Boundary conditions at the walls with thermionic electron emission in two temperature modeling of 'thermal' plasmas," Phys. Plasmas **22**, 083510 (2015).
[37]M. Lisnyak, M. D. Cunha, J. M. Bauchire, and M. S. Benilov, "Numerical modelling of high-pressure arc discharges: Matching the LTE arc core with the electrodes," J. Phys. D Appl. Phys. **50**, 315203 (2017).
[38]M. S. Benilov, L. G. Benilova, H.-P. Li, and G.-Q. Wu, "Sheath and arc-column voltages in high-pressure arc discharges," J. Phys. D Appl. Phys. **45**, 355201 (2012).
[39]P. Liang and J. P. Trelles, "3D numerical investigation of a free-burning argon arc with metal electrodes using a novel sheath coupling procedure," Plasma Sources Sci. Technol. **28**, 115012 (2019).
[40]S. M. Shkol'nik, "Anode phenomena in arc discharges: A review," Plasma Sources Sci. Technol. **20**, 013001 (2011).
[41]M. D. Campanell, "Negative plasma potential relative to electron-emitting surfaces," Phys. Rev. E **88**, 033103 (2013).
[42]M. D. Campanell and M. V. Umansky, "Strongly emitting surfaces unable to float below plasma potential," Phys. Rev. Lett. **116**, 085003 (2016).
[43]V. Vekselman, A. Khrabry, I. Kaganovich, B. Stratton, R. S. Selinsky, and Y. Raitses, "Quantitative imaging of carbon dimer precursor for nanomaterial synthesis in the carbon arc," Plasma Sources Sci. Technol. **27**, 025008 (2018).
[44]G. Cota-Sanchez, G. Soucy, A. Huczko, and H. Lange, "Induction plasma synthesis of fullerenes and nanotubes using carbon black–nickel particles," Carbon **43**, 3153 (2005).
[45]R. J. Thorn and G. H. Winslow, "Vaporization coefficient of graphite and composition of the equilibrium vapor," J. Chem. Phys. **26**, 186 (1957).
[46]J. Drowart, R. P. Burns, G. Demaria, and M. G. Inghram, "Mass spectrometric study of carbon vapor," J. Chem. Phys. **31**, 1131 (1959).
[47]R. E. Honig, "Mass spectrometric study of the molecular sublimation of graphite," J. Chem. Phys. **22**, 126 (1954).
[48]H. O. Pierson, *Handbook of Carbon, Graphite, Diamonds and Fullerenes* (Noyes Publications, Park Ridge, NJ, 1994), p. 419, ISBN: 978-0-8155-1339-1.
[49]B. R. Bird, W. E. Stewart, and E. N. Lightfoot, *Transport Phenomena* (Wiley, New York, 1960).
[50]R. J. W. Henry, P. G. Burke, and A. L. Sinfailam, "Scattering of electrons by C, N, O, N+, O+, and O++," Phys. Rev. **178**, 218 (1969).
[51]L. Jun-Bo, W. Yang, and Z. Ya-Jun, "Elastic cross sections for electron–carbon scattering," Chin. Phys. **16**, 72 (2007).
[52]V. A. Belyaev, B. G. Brezhnev, and E. M. Erastov, "Resonant charge transfer of low-energy carbon and nitrogen ions," Sov. Phys. JETP **27**, 924–926 (1968), available at http://www.jetp.ac.ru/cgi-bin/e/index/e/27/6/p924?a=list; http://www.jetp.ac.ru/cgi-bin/dn/e_027_06_0924.pdf.
[53]H. Suno and T. Kato, "Cross section database for carbon atoms and ions: Electron-impact ionization, excitation, and charge exchange in collisions with hydrogen atoms," At. Data Nucl. Data Tables **92**, 407–455 (2006).
[54]A. Ostrogorsky and C. Marin, "Heat transfer during production of carbon nanotubes by the electric-arc process," Heat Mass Transfer **42**, 470 (2006).
[55]R. W. Powell and F. H. Schofield, "The thermal and electrical conductivities of carbon and graphite to high temperatures," Proc. Phys. Soc. **51**, 153 (1939).